Seebeck Tuning in Chalcogenide Nanoplate Assemblies by Nanoscale Heterostructuring

Rutvik J. Mehta,[†] Chinnathambi Karthik,[†] Binay Singh,[†] Ranganath Teki,[†] Theo Borca-Tasciuc,[‡] and Ganpati Ramanath[†],*

[†]Department of Materials Science and Engineering and [‡]Department of Mechanical, Aerospace and Nuclear Engineering, Rensselaer Polytechnic Institute, 110 8th Street, Troy, New York 12180

ABSTRACT Chalcogenide nanostructures offer promise for obtaining nanomaterials with high electrical conductivity, low thermal conductivity, and high Seebeck coefficient. Here, we demonstrate a new approach of tuning the Seebeck coefficient of nanoplate assemblies of single-crystal pnictogen chalcogenides by heterostructuring the nanoplates with tellurium nanocrystals. We synthesized bismuth telluride and antimony telluride nanoplates decorated with tellurium nanorods and nanofins using a rapid, scalable, microwave-stimulated organic surfactant-directed technique. Heterostructuring permits two- to three-fold factorial tuning of the Seebeck coefficient, and yields a 40% higher value than the highest reported for bulk antimony telluride. Microscopy and spectroscopy analyses of the nanostructures suggest that Seebeck tunability arises from carrier-energy filtration effects at the Te—chalcogenide heterointerfaces. Our approach of heterostructuring nanoscale building blocks is attractive for realizing high figure-of-merit thermoelectric nanomaterials.

KEYWORDS: chalcogenide nanostructures · heterostructures · interfaces · Seebeck coefficient · thermoelectrics

Sculpting the dimensionality, that is, shape and size of semiconducting nanocrystals, is an attractive approach to obtain and tune material properties that are otherwise not observed in the bulk.[1] In addition, new functionalities and emergent properties can also be obtained by growing heterostructured nanocrystals comprising different materials with control over shape and size.[2−4] For instance, nanoscale heterostructures of semiconductors with metals[5−7] exhibit unique properties permitting novel electronic device designs[5] and also a system for artificial photosynthesis.[7] Here, we show that the Seebeck coefficient α of thin film assemblies of pnictogen chalcogenide nanoplates can be tuned by heterostructuring the nanoplates with tellurium, permitting larger α than achievable in corresponding bulk compounds or in assemblies of monolithic (nonheterostructured) nanoplates.

Bulk alloys based on semiconducting pnictogen chalcogenides, for example, Bi_2Te_3 and Sb_2Te_3, exhibit high room temperature figures of merit $ZT = (\alpha^2\sigma T)/\kappa \approx 1$, arising from a combination of a low band gap (*i.e.*, high electrical conductivity σ), large α, and low thermal conductivity κ.[8−10] Typically, κ, σ, and α in bulk thermoelectric materials are optimized by manipulating charge and heat carrier concentrations through alloying.[8] Theory predicts that quantum effects induced by nanostructuring[11] and introducing mechanisms to separate hot electrons[12] through use of material junctions or interfaces can increase α. However, such correlations are yet to be experimentally validated[13,14] in nanostructures and their assemblies. In fact, most of the experimentally demonstrated ZT increase in chalcogenide quantum dots,[15] thin film su-

perlattices,[16] and nanostructured bulk[17] have been shown to be mainly due to decreases in κ from size confinement.

Here, we show that the Seebeck coefficient of assemblies of single-crystal pnictogen chalcogenide nanoplates can be tuned by introducing tellurium nanocrystals of different shapes at the nanoplate edges. We demonstrate that heterostructuring with tellurium can be used to tune α of n-type Bi_2Te_3 between -35 and -110 $\mu V/K$, and increase α of p-type Sb_2Te_3 from 100 up to 150 $\mu V/K$, which is $\sim$40% higher than the highest values reported for bulk Sb_2Te_3.[9]

Pnictogen chalcogenide nanoplates were grown by a microwave-stimulated solvothermal synthesis in the presence of thioglycolic acid (TGA), which serves as shape-directing, surface-passivating, and sulfur-dopant delivery agent. In a typical reaction, we react thioligated bismuth or antimony, with either tri-*n*-octylphosphine ligated tellurium (TOP-Te) or telluric acid in the high-boiling pentanediol.[18]

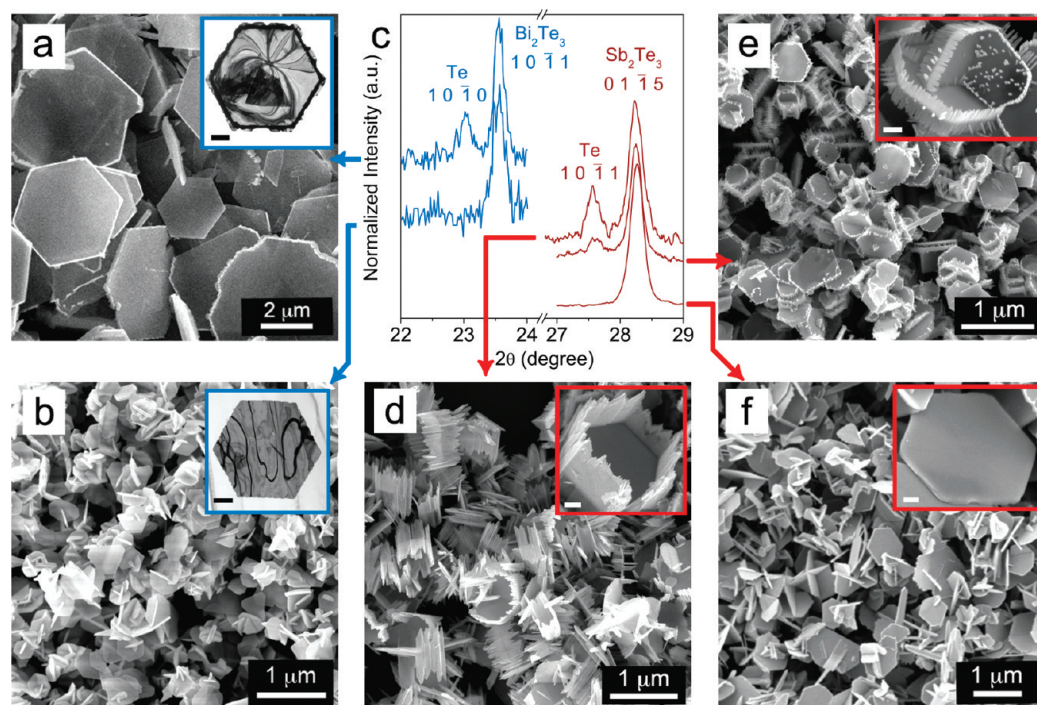**Figure 1.** SEM micrographs of assemblies of (a) Bi_2Te_3–Te heterostructures, (b) nonheterostructured Bi_2Te_3 nanoplates, (d and e) Sb_2Te_3–Te heterostructures, and (f) nonheterostructured Sb_2Te_3 nanoplates. Panel c shows X-ray diffractograms from the different samples (see arrows). The differing contrast at the plate edges in panels a, d, and e indicate Te. Insets are TEM images in panels a and b, and SEM images in panels d, e, and f with the scale bars denoting 100 nm.

The as-synthesized products are typically *ca.* 5−25 nm thick nanoplates with edge lengths tunable in the range of *ca.* 250−1200 nm (see Figure 1). Nanostructures of no other shapes were detectable, indicating excellent shape control. Bismuth telluride synthesis using telluric acid yields nanoplates with nanocrystal precipitates decorating the nanoplate edges, as indicated by the bright contrast in SEM images (*e.g.*, Figure 1a), and dark contrast in TEM images (inset). Changing the valence state of the Te precursor from Te^{6+} in telluric acid to Te^{2-} in TOP-Te suppresses such precipitation (see Figure 1b). X-ray diffractograms (Figure 1c and Supporting Information Figure S1) showing Bragg peaks from trigonal Te (space group $P3121$)[19] in addition to those from rhombohedral Bi_2Te_3 (space group $R\bar{3}m$)[18] suggest that the precipitates are Te nanocrystals. Altering the TGA concentration c_{TGA} during Bi_2Te_3 nanoplates syntheses using TOP-Te^{2-} does not produce Te nanocrystal precipitates.

In contrast to Bi_2Te_3 described above, Sb_2Te_3 nanoplate formation and heterostructuring are strongly dependent on c_{TGA}, and insensitive to the Te precursor used. We obtain nanoplates for $c_{TGA} > 0.2$ M; lower c_{TGA} yields irregularly shaped nanostructures. For 0.6 M < c_{TGA} < 0.8 M, we obtain hexagonal nanoplates with fin-like structures at plate edges (*e.g.*, see Figure 1d), while higher c_{TGA} values between 0.8 M < c_{TGA} < 2 M result in rod-like Te nanocrystals at plate perimeters as shown in Figure 1e. The dimensions and density of the Te nanocrystals decrease with increasing c_{TGA} (see Supporting Information Figure S3), as corroborated by the

Te $(10\bar{1}1)$ Bragg peak[18] intensity decrease relative to that of the Sb_2Te_3 $(10\bar{1}5)$ reflection (see Figure 1c and Supporting Information Figure S2). Te precipitation is completely suppressed for $c_{TGA} > 3$ M (see Figure 1f), consistent with X-ray diffractograms exhibiting only Sb_2Te_3 reflections, without any traces of Te peaks (see Figure 1c). Tellurium precipitation at low c_{TGA} and suppression at high c_{TGA} suggests that TGA acts as a reducing agent during antimony telluride synthesis. This inference is supported by the suppression of Te precipitation when nanoplate synthesis is carried out at low $c_{TGA} \approx 0.7$ M in the presence of even small quantities (*e.g.*, 0.1 M) of strong reducing agents such as hydrazine (see Supporting Information Figure S2).

The above results indicate that in the case of both the pnictogen chalcogenides, TGA mediates nanoplate formation through the reaction of thioligated antimony or bismuth with TOP-ligated tellurium ions. The strong role of the Te precursor for Bi_2Te_3–Te heterostructure formation, and the lack thereof for Sb_2Te_3–Te heterostructures, is attributable to the high reactivity of Bi^{3+} and Te^{2-} salts,[20] which tends to suppress $Te^{2-} \rightarrow Te^0$ oxidation. Substituting TOP-Te^{2-} with the higher valence state telluric acid opens up a new pathway for Te nanocrystal precipitation by $Te^{6+} \rightarrow Te^0$. In contrast, the relatively lower reactivity of Sb^{3+} and Te^{2-}[21] allows Te precipitation from Te^{2-} even under low oxidative conditions, rendering Te heterostructuring of Sb_2Te_3 insensitive to the oxidation state of Te in the precursor. The absence of homogeneous Te precipitation and the fact that the nanocrystals grow only on the nanoplate
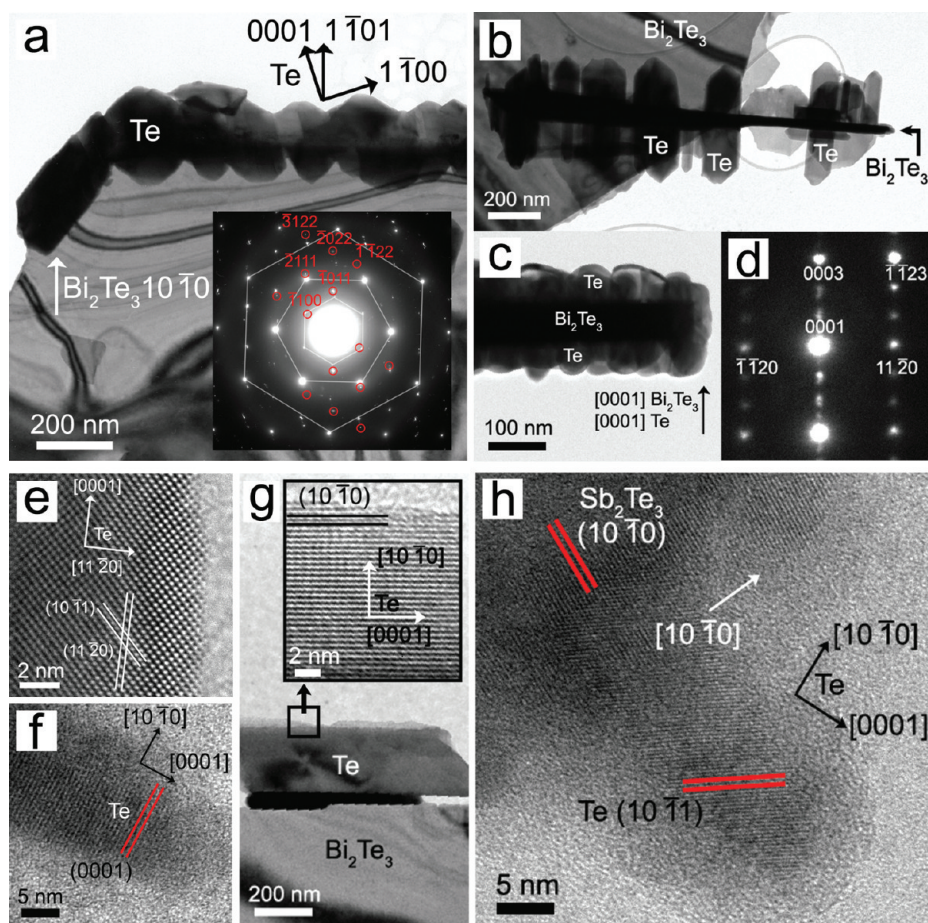
Figure 2. Representative TEM micrographs from a (a) Te-heterostructured Bi_2Te_3 nanoplate shown with a [0001] zone electron diffraction pattern (inset) exhibiting Bragg reflections from Bi_2Te_3 (hexagonal spot pattern) and Te (red circles); and (b) Bi_2Te_3−Te nanorod and (c) Bi_2Te_3−Te nanofin heterostructures with an edge-on view of the Bi_2Te_3 nanoplates. (d) Electron diffraction pattern from a Te nanocrystal at the plate edges. High resolution TEM micrograph from Te nanorods (e) parallel and (f) perpendicular to [0001] in the chalcogenide nanoplate. (g) Bright-field TEM image with a high resolution inset of a Te nanofin and (h) high resolution TEM micrograph taken at an Sb_2Te_3−Te interface.

edges suggest that Te nucleates and grows on select facets of the chalcogenide nanoplates, as corroborated by TEM results described below.

Bright-field TEM micrographs of individual nanoplates showing uniform contrast and spot diffraction patterns (see Figure 2a and insets in Figures 1a,b) confirm that hexagonally faceted nanoplates are single crystals. Energy dispersive X-ray spectroscopy (EDX) reveals that the nanoplates are nearly stoichiometric Bi_2Te_3 and Sb_2Te_3 within a 3 atom % uncertainty (see Supporting Information Figure S4). The plate shape is attributable to preferential growth along high charge carrier mobility [10$\bar{1}$0] and [11$\bar{2}$0] directions with prismatic {10$\bar{1}$0} bounding planes and inhibited growth along the low-thermal conductivity [0001] direction,[8,9] likely by a ledge growth mechanism.[10] We note that the large in-plane dimensionality along the high charge carrier mobility directions and the nanoplate thickness being comparable to the phonon mean free path are conducive for high electrical conductivity and low thermal conductivity, respectively, and hence higher ZT values. Tellurium nanocrystals precipitate exclusively from nano-

plate (10$\bar{1}$0) bounding edges as fins or rods in configurations that are either perpendicular or parallel to basal (0001) planes in the chalcogenide nanoplates (see Figures 2a−c). No Te precipitation was observable on the (0001) faces. Electron diffraction (Figure 2d) and high-resolution TEM (Figures 2e−h) analyses confirm that the Te nanocrystals grow along Te [0001], taking on one of the following two orientation relationships with the chalcogenide nanoplate crystals: $(0001)_{Te}\|(0001)_{chalcogenide}$ and $[0001]_{Te}\|[0001]_{chalcogenide}$, and $(0001)_{Te}\|(10\bar{1}0)_{chalcogenide}$ and Te $[10\bar{1}0]_{Te}\|[10\bar{1}0]_{chalcogenide}$. The Te fins and rods have similar crystallography (Figures 2b,c), but differ in size and frequency. High resolution TEM reveals epitaxy at the Te-chalcogenide interfaces (Figure 2h), which is the likely reason for the selective heterostructuring at the plate edges in exclusion to the plate faces. The differences in heterostructure morphology, for example, prismatic shape of the Te nanocrystals on Bi_2Te_3 compared with the smaller needle-like Te on Sb_2Te_3, could be due to the lattice mismatch difference between Te and Bi_2Te_3 (∼1.5%) and Te and Sb_2Te_3 (∼4.4%).
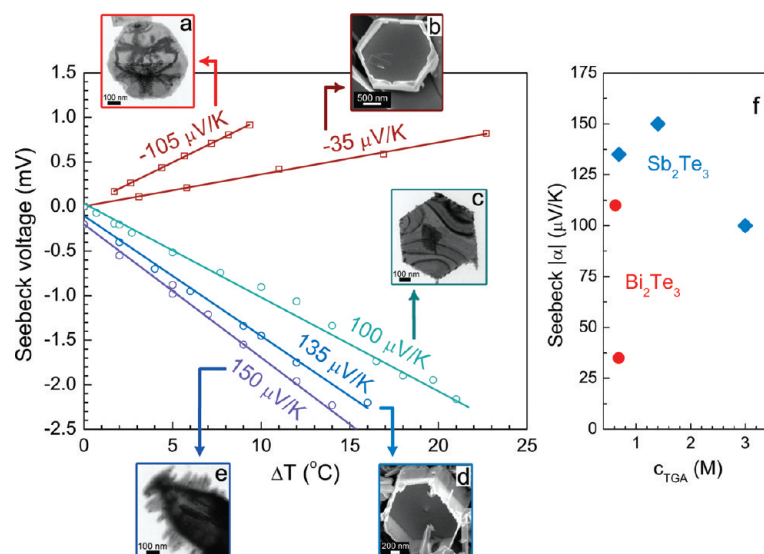
Figure 3. Seebeck voltage plotted as a function of the temperature gradient ΔT across thin film assemblies of (a) Bi_2Te_3 nanoplates, (b) Bi_2Te_3—Te heterostructures, (c) Sb_2Te_3 nanoplates, (d) Sb_2Te_3—Te nanofin heterostructures, and (e) Sb_2Te_3—Te nanorod heterostructures. For each sample, the value of the Seebeck coefficient α and a representative TEM (a, c, and e) and SEM (b and d) micrograph depicting the nanoplate/heterostructure morphology are shown. (f) The absolute value of the Seebeck coefficient α plotted as a function of TGA concentration c_{TGA} used in the syntheses of Bi_2Te_3 (filled circles) and Sb_2Te_3 (filled diamonds) nanoplates and their heterostructures.

Figure 3 summarizes the results of Seebeck coefficient measurements on thin film assemblies of the nanoplates or nanoplate heterostructures. The nanoplates were drop-cast into micrometer-thick films on patterned electrode and heater structures (see inset). The as-prepared thin film assemblies were insulating with four-probe sheet resistances $R_s > 100$ MΩ/sq likely due to poor nanoplate packing, high porosity, and TGA capping. Annealing the nanoplate films at 250 °C or chemical cleaning in 10% hydrazine[22] decreased R_s to *ca.* 0.1—1000 kΩ/sq attributable to better interplate contact, with no observable changes in the nanostructure morphology.

Thin film assemblies of Bi_2Te_3 nanoplates and Bi_2Te_3—Te heterostructures exhibit $\alpha < 0$, indicative of n-type behavior. This majority carrier reversal with reference to the behavior of bulk bismuth telluride is consistent with TGA-induced sulfur doping reported earlier.[23−25] The amount of sulfur in the Bi_2Te_3-based nanostructures is below the EDX detection limit, implying that subatomic percent concentrations are enough to cause the carrier reversal. Heterostructuring the nanoplates with Te nanocrystals decreases α from *ca.* −110 μV/K observed for single-phase nanoplates, to α *ca.* −35 μV/K for Bi_2Te_3—Te heterostructures. In contrast, Sb_2Te_3 nanoplate and Sb_2Te_3—Te heterostructure assemblies show p-type behavior ($\alpha > 0$) consistent with that seen in bulk Sb_2Te_3.[8−10] Sulfur-induced carrier reversal is probably ineffective in Sb_2Te_3 due to the generation of self-compensating antimony antisite defects.[8,9] Unlike Bi_2Te_3, Te-heterostructuring of Sb_2Te_3 plates increases α from ~100 μV/K observed in single-phase nanoplate assemblies. Thin film assemblies of Sb_2Te_3—Te nanofin heterostructures show $\alpha \approx 135$

μV/K while those with Te nanorods exhibit $\alpha \approx 150$ μV/K. Both these values are higher than the highest α of ~110 μV/K reported for single crystal bulk Sb_2Te_3.[9]

We propose that the observed changes in Seebeck coefficient are mainly due to Te heterostructuring. Since Te enrichment is known[9,10] not to increase α in bulk Sb_2Te_3 beyond 110 μV/K we attribute the observed increase in α to favorable energy filtration effects at the Sb_2Te_3—Te junctions in the nanoplates, and their assemblies. Charge carriers with energies lower than a threshold value would be blocked,[26] raising the average carrier energy and hence α, as suggested elsewhere.[12,27] Since Te is a p-type metalloid, we expect Te heterostructuring with n-Bi_2Te_3 to diminish α, while Te heterostructuring with p-Sb_2Te_3 would enhance α, as observed. Although sulfur incorporation causes majority carrier charge reversal in Bi_2Te_3, we do not expect sulfur to be a major contributor to the change in Seebeck coefficient. This hypothesis is supported by the fact that both Bi_2Te_3 nanoplates and Bi_2Te_3—Te heterostructures are synthesized under identical TGA concentrations (see Figure 3f). Furthermore, for Sb_2Te_3, decreasing c_{TGA} increases Te nanocrystal formation (Supporting Information Figure S2) and increases α, contrary to what would be expected if sulfur incorporation were the major mechanism. The nonmonotonic increase in α with c_{TGA} (Figure 3f) could be due to carrier concentration changes resulting from an interplay between sulfur incorporation and compensating defect generation, which needs further study.

In summary, heterostructures of tellurium-decorated single-crystal pnictogen chalcogenide nanoplates were controllably fabricated by a rapid, scalable synthetic microwave-chemistry technique. Te heterostructuring

provides a means to factorially tune the Seebeck coefficient α for n-type as well as p-type chalcogenides. Thin film assemblies of Te-heterostructured Sb_2Te_3 nanoplates exhibit ~40% higher α than the maximum reported value for bulk Sb_2Te_3. Our microscopy and spectroscopy analyses suggest that energy filtration of charge carriers at Te—chalcogenide interfaces is the likely mechanism of heterostructuring-induced changes in α. Heterostructuring nanoscopic building blocks provides an additional degree of freedom that is unavailable in bulk to enhance thermoelectric properties. Heterostructuring could also conceivably increase ZT by decreasing κ due to enhanced phonon scattering at the heterointerfaces.

METHODS AND EXPERIMENTAL DETAILS

Heterostructure Synthesis. Thioglycolic acid ($CH_2COOHSH$, 95%), anhydrous bismuth chloride ($BiCl_3$), antimony chloride ($SbCl_3$), 1,5-pentanediol (95%), technical grade tri-*n*-octylphosphine (TOP), 200 mesh tellurium shots, and telluric acid were obtained from Sigma Aldrich and used without further purification. In a typical small-scale synthesis, 10 mg of tellurium (~0.08 mmol) was added to 2—5 mL TOP and heated in the microwave oven for 90—120 s to obtain a colorless to faint yellow TOP—Te complex. Alternately for the Bi_2Te_3—Te heterostructures, telluric acid was added to pentanediol and irradiated in the microwave oven for 30—60 s. A Bi (or Sb) chloride solution was prepared by adding 13 mg (~0.04 mmol) of $BiCl_3$ or 10 mg (~0.04 mmol) $SbCl_3$ to 2.5—10 mL 1,5-pentanediol followed by sonication for 15 min. The desired volume of thioglycolic acid (typically 100—750 μL) was added to the Bi (or Sb) pentanediol solution. The solutions with Te and thioligated Bi (or Sb) were mixed and microwaved for *ca.* 30—60 s in a domestic Panasonic microwave oven rated at 1250 W.

Film Fabrication. Micrometer-thick thin film assemblies of the nanoplate films were fabricated by drop-casting or dip-coating the nanocrystal dispersions in organic solvents onto prepatterned glass slides. To obtain films with reasonable electrical conductivity values, the film assemblies were either annealed at 250 °C for 90—120 min or chemically cleaned by treating with a solution of 10% hydrazine in acetonitrile prior to film deposition.

Materials Characterization. Films formed by drop-casting the nanoplates onto glass slides, silicon wafer, or TEM grids were characterized by X-ray diffractometry (XRD), scanning and transmission electron microscopy (SEM and TEM) and diffraction, and X-ray photoelectron spectroscopy (XPS). A Bruker D-8 instrument with a Cu Kα probe beam was used for XRD. The nanoplate morphology and structure were determined using a field-emission Zeiss Supra 55 SEM operated at 1—5 kV, a Philips CM 12 TEM operated at 120 kV, and a JEOL 2010 TEM operated at 200 kV.

Thermoelectric Transport Characterization. We used fabricated electrical circuits for film electrical conductivity and Seebeck coefficient measurements. The electrical circuits were made by lithographic patterning of gold electrodes on glass slides by a lift-off technique. Electrical conductivity σ was measured using a four-probe test system. The Seebeck voltage was measured across the nanoplate assembly between two gold electrodes, across which a temperature gradient was established by passing current through a thin film heater with the other end attached to a heat sink. The temperatures were measured by placing precalibrated thermistors or thermocouples near the electrodes.

Supporting Information Available: X-ray diffractograms and X-ray spectra with additional electron micrographs. This material is available free of charge *via* the Internet at http://pubs.acs.org.

REFERENCES AND NOTES

1. Acharya, S.; Sarma, D. D.; Golan, Y.; Sengupta, S.; Ariga, K. Shape-Dependent Confinement in Ultrasmall Zero-, One-, and Two-Dimensional PbS Nanostructures. *J. Am. Chem. Soc.* **2009**, *131*, 11282–11283.
2. Mokari, T.; Rothenberg, E.; Popov, I.; Costi, R.; Banin, U. Selective Growth of Metal Tips onto Semiconductor Quantum Rods and Tetrapods. *Science* **2004**, *304*, 1787–1790.
3. Cozzoli, P. D.; Pellegrino, T.; Manna, L. Synthesis, Properties and Perspectives of Hybrid Nanocrystal Structures. *Chem. Soc. Rev.* **2006**, *35*, 1195–1208.
4. Milliron, D. J.; Hughes, S. M.; Cui, Y.; Manna, L.; Li, J. B.; Wang, L. W.; Alivisatos, A. P. Colloidal Nanocrystal Heterostructures with Linear and Branched Topology. *Nature* **2004**, *430*, 190–195.
5. Lauhon, L. J.; Gudiksen, M. S.; Wang, C. L.; Lieber, C. M. Epitaxial Core—Shell and Core—Multishell Nanowire Heterostructures. *Nature* **2002**, *420*, 57–61.
6. Sun, Z. H.; Yang, Z.; Zhou, J. H.; Yeung, M. H.; Ni, W. H.; Wu, H. K.; Wang, J. F. A General Approach to the Synthesis of Gold-Metal Sulfide Core—Shell and Heterostructures. *Angew. Chem., Int. Ed.* **2009**, *48*, 2881–2885.
7. Tada, H.; Mitsui, T.; Kiyonaga, T.; Akita, T.; Tanaka, K. All-Solid-State Z-Scheme in CdS—Au—TiO_2 Three-Component Nanojunction System. *Nat. Mater.* **2006**, *5*, 782–786.
8. Nolas, G. S.; Sharp, J.; Goldsmid, H. J. Thermoelectrics: Basic Principles and New Materials Developments; Springer: New York, 2001; pp 111–131.
9. Rowe, D. M. CRC Handbook of Thermoelectrics; CRC Press: Boca Raton, FL, 1995; pp 211–236.
10. Rowe, D. M., *Thermoelectrics Handbook: Macro to Nano*. CRC: 2005; pp 25–1-27–18.
11. Dresselhaus, M. S.; Chen, G.; Tang, M. Y.; Yang, R. G.; Lee, H.; Wang, D. Z.; Ren, Z. F.; Fleurial, J. P.; Gogna, P. New Directions for Low-Dimensional Thermoelectric Materials. *Adv. Mater.* **2007**, *19*, 1043–1053.
12. Minnich, A. J.; Dresselhaus, M. S.; Ren, Z. F.; Chen, G. Bulk Nanostructured Thermoelectric Materials: Current Research and Future Prospects. *Energy Environ. Sci.* **2009**, *2*, 466–479.
13. Heremans, J. P.; Thrush, C. M.; Morelli, D. T. Thermopower Enhancement in Lead Telluride Nanostructures. *Phys. Rev. B* **2004**, *70*, 115334.
14. Zide, J. M. O.; Vashaee, D.; Bian, Z. X.; Zeng, G.; Bowers, J. E.; Shakouri, A.; Gossard, A. C. Demonstration of Electron Filtering to Increase the Seebeck Coefficient in $In_{0.53}Ga_{0.47}As/In_{0.53}Ga_{0.28}Al_{0.19}$ as Superlattices. *Phys. Rev. B* **2006**, *74*, 205335.
15. Harman, T. C.; Taylor, P. J.; Walsh, M. P.; LaForge, B. E. Quantum Dot Superlattice Thermoelectric Materials and Devices. *Science* **2002**, *297*, 2229–2232.
16. Venkatasubramanian, R.; Siivola, E.; Colpitts, T.; O'Quinn, B. Thin-Film Thermoelectric Devices with High Room-Temperature Figures of Merit. *Nature* **2001**, *413*, 597–602.
17. Poudel, B.; Hao, Q.; Ma, Y.; Lan, Y. C.; Minnich, A.; Yu, B.; Yan, X.; Wang, D. Z.; Muto, A.; Vashaee, D.; *et al.* High-Thermoelectric Performance of Nanostructured Bismuth Antimony Telluride Bulk Alloys. *Science* **2008**, *320*, 634–638.
18. 1,5-Pentanediol boils at 240—242 °C.
19. See JCPDS file 15-874 for antimony telluride, JCPDS file 15-863 for bismuth telluride, and JCPDS 36-1452 for tellurium.

20. Scheele, M.; Oeschler, N.; Meier, K.; Kornowski, A.; Klinke, C.; Weller, H. Synthesis and Thermoelectric Characterization of Bi$_2$Te$_3$ Nanoparticles. *Adv. Funct. Mater.* **2009**, *19*, 3476–3483.

21. Lide, D. R. *CRC Handbook of Chemistry and Physics*, 88th ed.; CRC Press/Taylor and Francis: Boca Raton, FL, 2008; pp 8-23−8-24.

22. Prolonged annealing of the heterostructure films at *ca.* 250−300 °C leads to irreversible morphological changes through Te diffusion resulting in partial and/or complete dissolution of Te nanocrystals and Te enrichment of the pnictogen chalcogenide nanoplates resulting in voided and patterned hexagonal nanoplates. Hence we use chemical cleaning.

23. Horak, J.; Lostak, P.; Koudelka, L.; Novotny, R. Inversion of Conductivity Type in Bi$_2$Te$_{3-x}$S$_x$ Crystals. *Solid State Commun.* **1985**, *55*, 1031–1034.

24. Purkayastha, A.; Kim, S.; Gandhi, D. D.; Ganesan, P. G.; Borca-Tasciuc, T.; Ramanath, G. Molecularly Protected Bismuth Telluride Nanoparticles: Microemulsion Synthesis and Thermoelectric Transport Properties. *Adv. Mater.* **2006**, *18*, 2958–2963.

25. Purkayastha, A.; Lupo, F.; Kim, S.; Borca-Tasciuc, T.; Ramanath, G. Low-Temperature, Template-Free Synthesis of Single-Crystal Bismuth Telluride Nanorods. *Adv. Mater.* **2006**, *18*, 496–500.

26. The band gaps of tellurium, bismuth telluride, and antimony telluride are ∼0.3, ∼0.16, and ∼0.3 eV, respectively. The exact band structure details of Te−chalcogenide heterostructure junctions are not yet known.

27. Vashaee, D.; Shakouri, A. Improved Thermoelectric Power Factor in Metal-Based Superlattices. *Phys. Rev. Lett.* **2004**, *92*, 106013.